

An Electron/Ion Dual Conductive Integrated Cathode Using Cationic/Anionic Redox for High-Energy-Density All-Solid-State Lithium-Sulfur Batteries

Wenli Pan,^[a] Kentaro Yamamoto,*^[a] Toshiyuki Matsunaga,^[a] Toshiki Watanabe,^[a] Mukesh Kumar,^[a] Neha Thakur,^[a] Tomoki Uchiyama,^[a] Masayuki Uesugi,^[b] Akihisa Takeuchi,^[b] Atsushi Sakuda,^[c] Akitoshi Hayashi,^[c] Masahiro Tatsumisago,^[c] and Yoshiharu Uchimoto^[a]

All-solid-state lithium-sulfur batteries (ASSLSB), composed of sulfur cathode and lithium metal anode with high theoretical capacity, have a potentially higher energy density by weight than a typical lithium-ion battery (LIB). However, due to insulating sulfur, a relatively large proportion of electronic (carbon) and ionic (solid electrolyte) conductors are mixed for cathode fabrication, leading to inferior practical capacity. Herein, we report a novel integrated cathode $\text{Li}_2\text{S}-\text{LiI}-\text{MoS}_2$ which has relatively high electronic and ionic conductivities (the order of $10^{-4} \text{ S cm}^{-1}$) without any carbon and solid electrolyte. The ASSLSB with integrated $\text{Li}_2\text{S}-\text{LiI}-\text{MoS}_2$ cathode delivers a remarkably high energy density of 1020 Wh kg^{-1} at the cathode level

at room temperature. By applying precise X-ray diffraction, pair distribution function analysis and X-ray computed tomography, it is found that the formation of an ionic conducting phase composed mainly of LiI during discharge is responsible for the high rate capability. Furthermore, X-ray absorption fine structure (XAFS) has also revealed the charge compensation mechanism and ascertained the involvement of both Mo 3d and S 3p orbitals during the charging and discharging process. It is believed the strategy will pave the way for developing high practical energy density at room temperature for all-solid-state batteries.

Introduction

Power sources with high gravimetric energy density are critical elements in cutting-edge technologies for aircraft and drone applications. Among the numerous energy storage systems, all-solid-state lithium-sulfur batteries (ASSLSBs) have drawn much attention due to the remarkably high theoretical energy density ($> 2000 \text{ Wh kg}^{-1}$), which is generated by both high theoretical capacity of S (1675 mAh g^{-1}) or Li_2S (1167 mAh g^{-1}) as cathode and lithium metal (3860 mAh g^{-1}) as anode.^[1] This battery also has the advantage of being inexpensive because it uses sulfur, which is an abundant resource, as its cathode, and is expected to be expanded into applications such as stationary storage batteries. Besides, compared to liquid system, solid electrolytes could block the shuttle effect and provide higher safety.^[2]

Although ASSLSBs promise to exceed the theoretical energy density of typical LIBs, the practical performance is far from satisfied, most notably in energy density. Sulfur and the discharge product Li_2S have low ionic and electronic conductivity and must be mixed with solid electrolyte and carbon materials when forming a composite electrode. To realize lithium-ion and/or electron transport, a significant fraction of non-active solid electrolytes and carbon need to be added into the cathode composite, which dilutes the energy density largely.^[3] Specifically, it is common to use sulfide-based solid electrolytes (SSE) with high ionic conductivity, such as Li_3PS_4 , $\text{Li}_{10}\text{GeP}_2\text{S}_{12}$ and lithium argyrodite $\text{Li}_x\text{PS}_5\text{X}$ ($\text{X}=\text{Cl}, \text{Br}$) and high electronic conductivity carbon materials, such as acetylene black (AB), Ketjenblack (KB) and vapor grown carbon fiber (VGCF) as conductive additives.^[4] And these non-active conductive additives usually account for 50% to 75% of the cathode mass and lead to low active material content.^[5]

To fill the gap between the theoretical and practical energy density of ASSLSBs, much effort has been put into constructing ionic and electronic pathways in the cathode composite more effectively. As doping with lithium halides LiX ($\text{X}=\text{Cl}, \text{Br}, \text{I}$) in sulfide active material is an effective way to improve ionic conductivity and electrochemical stability.^[6] With LiI doping, the ionic conductivity of $\text{Li}_2\text{S}-\text{LiI}$ is improved to $10^{-6} \text{ S cm}^{-1}$, which is two orders of magnitude higher than that of Li_2S .^[7] The content of Li_2S in the cathode composite could be promoted, which results from the reduced $\text{Li}^+/\text{S}^{2-}$ interaction and enhanced rate capability.^[8] However, lithium halides are non-electroactive species and the rate capability is improved at the expense of specific capacity. To reduce non-active conductors further, the

[a] W. Pan, Dr. K. Yamamoto, Dr. T. Matsunaga, Dr. T. Watanabe, Dr. M. Kumar, Dr. N. Thakur, Dr. T. Uchiyama, Prof. Dr. Y. Uchimoto Graduate School of Human and Environmental Studies Kyoto University Yoshida-nihonmatsu-cho, Sakyo, Kyoto, 606-8501 (Japan)
E-mail: k.yamamoto@cc.nara-wu.ac.jp

[b] Dr. M. Uesugi, Dr. A. Takeuchi Japan Synchrotron Radiation Research Institute (JASRI) Kouto, Sayo-cho, Sayo-gun, Hyogo, 679-5198 (Japan)

[c] Dr. A. Sakuda, Prof. Dr. A. Hayashi, Prof. Dr. M. Tatsumisago Department of Applied Chemistry Graduate School of Engineering, Osaka Metropolitan University Sakai, Osaka, 599-8531 (Japan)

 Supporting information for this article is available on the WWW under <https://doi.org/10.1002/batt.202300427>

ideal alternatives should have not only good electronic conductivity, but also rich Li⁺ storage sites and good Li⁺ diffusion property.^[9] In that context, transition metal sulfides have been reported to substitute carbon partially or totally, such as FeS₂ and VS₂, leading to a capacity between 350 to 400 mAh g⁻¹ based on whole cathode mass.^[10] S-Mo₆S₈ cathode is reported to remove all non-active additives in cathode composite, achieving an overall cathode capacity of 483 mAh g⁻¹ at 70 °C, with the energy densities of 777 Wh kg⁻¹ correspondingly.^[11] While the active material content is improved, the fully conductor-substituted cathode materials still show limited performance, especially at room temperature. Therefore, it is challenging and significant to realize the cathode without carbon and SSE at room temperature, and the specific capacity as well as energy density at the cathode level remains to be improved further.

Herein, to address the abovementioned issues, we developed an integrated cathode Li₂S-Lil-MoS₂ without any carbon and SSE in composite, where Li₂S-Lil solid solution and metallic (1T) Li_xMoS₂ provide good electron/ion dual conductivity. Benefiting from its entire electronic/ionic network, the Li₂S-Lil-MoS₂ cathode plays dual-function roles of both delivering capacity and conducting electron/ion by itself. Comprehensive and advanced analytical techniques, especially synchrotron X-ray absorption spectroscopy (XAS), high-energy X-ray diffraction and pair distribution function analysis, and X-ray computed tomography, have revealed the origin of the excellent electrode properties of the developed materials.

Results and Discussion

Optimization and phase characterization

A series of Li₂S-Lil-MoS₂ samples using Li₂S, Lil and MoS₂ as raw materials were synthesized by a one-step ball-milling method. As the performance of the cathode in all-solid-state batteries is usually limited by ion transport,^[12] the proportion of Lil was firstly optimized to improve ionic conductivity, as (1-x)Li₂S-xLil ($x=0.05, 0.1, 0.15, 0.2, 0.25$). The synchrotron XRD patterns, corresponding lattice constants and iodine occupancy in Li₂S structure obtained from Rietveld refinement are shown in Figure 1a–c and Figure S1. As depicted in Figure 1a, the hump at a low angle of about 6.8° is probably due to the halo signal from the glassy capillaries, which are holders of samples for Synchrotron XRD. With a low Lil content of 5 mol%, the lattice constant is 5.744 Å, larger than pure Li₂S (5.718 Å), which is because larger iodine ions partially occupy the site of sulfur ions. As for the sample with $x \leq 0.2$, all peaks were assigned to Li₂S (space group: Fm $\bar{3}m$) while peaks attributed to Lil appeared in the sample with $x=0.25$. Both the lattice constants based on the Li₂S phase and iodine occupancy in Li₂S structure increased linearly with Lil content until $x=0.2$ and did not change over $x=0.25$. These results suggest Li₂S-Lil solid solution phase is obtained by ball milling method and the limit of solid solubility is $x=0.2$. At the composition of $x=0.2$, the sample showed

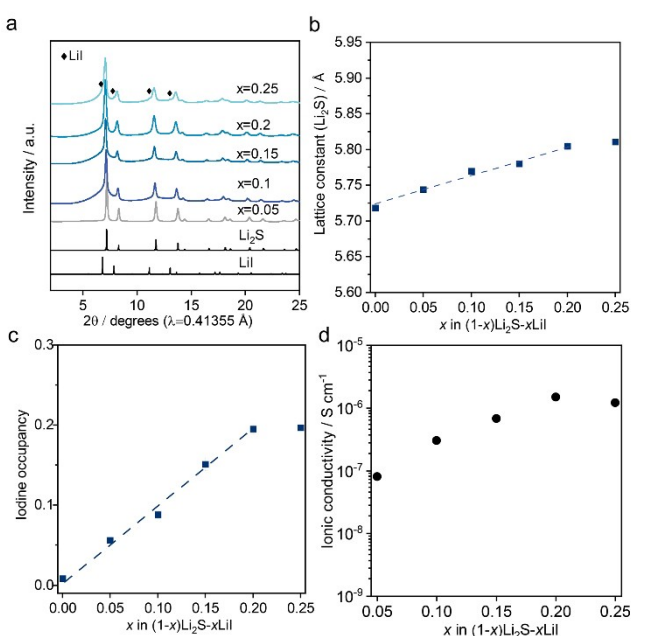


Figure 1. (a) The synchrotron XRD patterns for (1-x)Li₂S-xLil ($x=0.05, 0.1, 0.15, 0.2, 0.25$) with comparison of Li₂S and Lil as raw materials. The clubs correspond to Lil. (b) The lattice constant ($a=b=c$) of the main phase in (1-x)Li₂S-xLil. (c) The iodine occupancy in Li₂S structure of (1-x)Li₂S-xLil . (d) The ionic conductivities of (1-x)Li₂S-xLil at 25 °C.

highest ionic conductivity of 1.5×10^{-6} S cm⁻¹ at 25 °C (Figure 1c), which was in good agreement with previous report.^[7]

With optimal composition of Lil ($x=0.2$), the proportion of MoS₂, (1-y)(0.8Li₂S-0.2Lil)-yMoS₂ ($y=0, 0.05, 0.1, 0.15, 0.2$) was optimized further. Synchrotron XRD and Rietveld refinement were performed for samples to identify phases of the samples and to calculate the corresponding lattice constants (Figure 2a, 2b, S2). In the as-prepared cathodes of (1-y)(0.8Li₂S-0.2Lil)-yMoS₂ ($y=0, 0.05, 0.1$), all peaks were assigned to Li₂S (space group: Fm $\bar{3}m$). In contrast to these samples, broad peaks appeared around 3.7, 8.9, and 15.1° in addition to the peaks attributed to Li₂S in the as-prepared cathodes of (1-y)(0.8Li₂S-0.2Lil)-yMoS₂ ($y=0.15, 0.2$). The peak positions were close to the starting material 2H-MoS₂ ($P6_3/mmc$) and 1T-MoS₂ ($P\bar{3}m1$). Due to the weak and broad reflection, it is impractical to identify the origin of the peaks only with the XRD patterns. Therefore, we used further analytical techniques to examine it as discussed later. The lattice constant of Li₂S phase in the (1-y)(0.8Li₂S-0.2Lil)-yMoS₂ was larger than Li₂S because Lil was doped in Li₂S structure (Figure 1a, b) and remained unchanged with increasing MoS₂ contents (Figure 2b). These results indicate that the Mo cation was not doped in the Li₂S structure. The electronic and ionic conductivities were significantly improved with increase of MoS₂ contents (Figure 2c and d). Especially when $y=0.1, 0.15$ and 0.2 , electronic and ionic conductivities were higher than 1×10^{-4} S cm⁻¹, which are possibly capable of being cathode materials without other conductive additives. To confirm that, charge / discharge measurements of the (1-y)(0.8Li₂S-0.2Lil)-yMoS₂ were performed as shown in Figure S6. When $x=0.2$ of Lil and $y=0.15$ of MoS₂, the cathode delivered

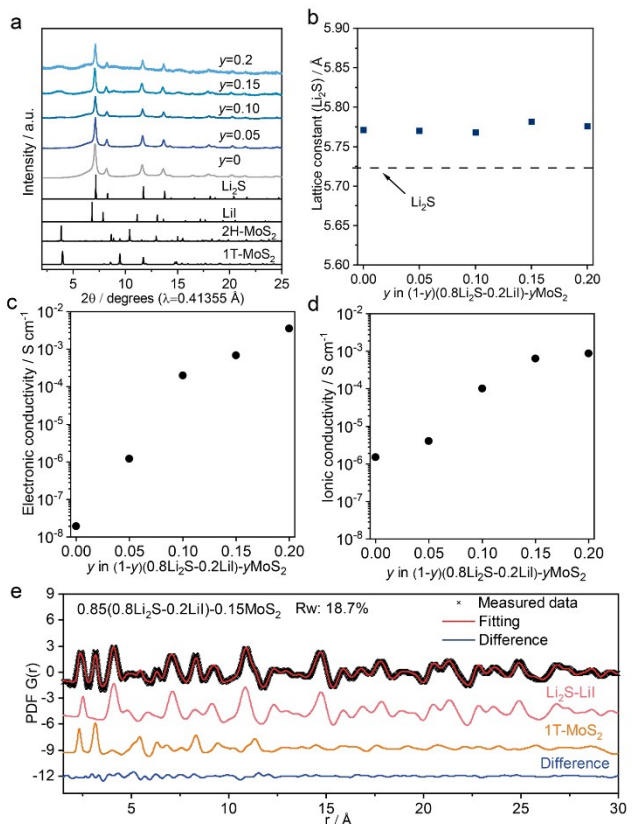


Figure 2. The phase characterization of $\text{Li}_2\text{S}-\text{LiL}-\text{MoS}_2$. (a) Synchrotron XRD patterns of ball-milling products $(1-y)(0.8\text{Li}_2\text{S}-0.2\text{LiL})-\text{yMoS}_2$ ($y=0, 0.05, 0.1, 0.15, 0.2$) with comparison of Li_2S , LiL and $2\text{H}-\text{MoS}_2$ ($P6_3/mmc$) as raw materials. The XRD pattern of $1\text{T}-\text{MoS}_2$ ($P3m1$) is simulated from cif file of $1\text{T}-\text{MoS}_2$ by Fullprof. (b) Lattice constants of Li_2S phase in $(1-y)(0.8\text{Li}_2\text{S}-0.2\text{LiL})-\text{yMoS}_2$, (c) Electronic and (d) Ionic conductivities of $(1-y)(0.8\text{Li}_2\text{S}-0.2\text{LiL})-\text{yMoS}_2$. (e) PDF result of $0.85(0.8\text{Li}_2\text{S}-0.2\text{LiL})-0.15\text{MoS}_2$.

highest discharge capacity over 500 mAh g^{-1} with the current density of 25 mA g^{-1} at 25°C . Consequently, further experiments were performed for the $0.85(0.8\text{Li}_2\text{S}-0.2\text{LiL})-0.15\text{MoS}_2$ as the optimized one. To examine the structure of the $0.85(0.8\text{Li}_2\text{S}-0.2\text{LiL})-0.15\text{MoS}_2$, Raman spectroscopy, Pair distribution function (PDF) analysis and S K-edge XANES measurement with linear combination fitting were conducted for it.

As shown in Raman spectra (Figure S3), the $0.85(0.8\text{Li}_2\text{S}-0.2\text{LiL})-0.15\text{MoS}_2$ did not exhibit peaks at 378 cm^{-1} and 404 cm^{-1} , which are attributed to E_{2g} and A_{1g} modes in the starting material MoS_2 (2H-phase), but exhibited two peaks at $\sim 150 \text{ cm}^{-1}$ and 220 cm^{-1} , marked as J_1 and J_2 respectively. The peak positions were in good agreement with those of MoS_2 with 1T-phase,^[13] indicating that 1T-phase MoS_2 was formed in the $0.85(0.8\text{Li}_2\text{S}-0.2\text{LiL})-0.15\text{MoS}_2$. To confirm the existence of 1T-phase MoS_2 in the bulk of $0.85(0.8\text{Li}_2\text{S}-0.2\text{LiL})-0.15\text{MoS}_2$, the PDF analysis was performed (Figure 2e and S4). The refinement of PDF for $0.85(0.8\text{Li}_2\text{S}-0.2\text{LiL})-0.15\text{MoS}_2$ fitting with 1T-phase MoS_2 showed better result ($Rw: 18.7\%$) than fitting with 2H- MoS_2 ($Rw: 23.5\%$),^[13c] indicating that 1T-phase MoS_2 exists in the bulk of $0.85(0.8\text{Li}_2\text{S}-0.2\text{LiL})-0.15\text{MoS}_2$. The electronic structure of S in the $0.85(0.8\text{Li}_2\text{S}-0.2\text{LiL})-0.15\text{MoS}_2$ was examined by S K-edge

XANES measurement with linear combination fitting (Figure S5). The fitting result with polysulfide was better than that without polysulfide, indicating that phase transition from Li_2S to polysulfide with delithiation occurred in the $0.85(0.8\text{Li}_2\text{S}-0.2\text{LiL})-0.15\text{MoS}_2$. This result was in agreement with the no change of lattice constant of Li_2S with increase of MoS_2 content (Figure 2b). Since it has been 2H-phase MoS_2 undergoes a phase transition to 1T-phase MoS_2 when Li^+ is inserted,^[14] the 1T-phase MoS_2 and polysulfide formation observed in the $0.85(0.8\text{Li}_2\text{S}-0.2\text{LiL})-0.15\text{MoS}_2$ suggest that Li^+ in Li_2S was inserted into 2H-phase MoS_2 by ball milling, forming 1T-phase Li_xMoS_2 . It has been reported that 1T-phase MoS_2 has high electronic conductivity and that 1T-phase Li_xMoS_2 is capable of Li^+ insertion and extraction.^[14-15] Therefore, in the $(1-y)(0.8\text{Li}_2\text{S}-0.2\text{LiL})-\text{yMoS}_2$, the increasing amount of 1T-phase Li_xMoS_2 with increasing the MoS_2 content improved the electronic and ionic conductivities (Figure 2c, d).

Electrochemical performance

Electrochemical performances of the optimized $\text{Li}_2\text{S}-\text{LiL}-\text{MoS}_2$ ($0.85(0.8\text{Li}_2\text{S}-0.2\text{LiL})-0.15\text{MoS}_2$) as the integrated cathode without any carbon or SSE was further examined. As for galvanostatic charge-discharge at 25°C in Figure 3a, the $0.85(0.8\text{Li}_2\text{S}-0.2\text{LiL})-0.15\text{MoS}_2$ showed a capacity of 349 mAh g^{-1} at 25 mA g^{-1} , with a voltage plateau of 2.6 V in the first charge. In the first discharge, $0.85(0.8\text{Li}_2\text{S}-0.2\text{LiL})-0.15\text{MoS}_2$ cathode showed a capacity of 491 mAh g^{-1} . Among subsequent a few cycles, the polarization of $0.85(0.8\text{Li}_2\text{S}-0.2\text{LiL})-0.15\text{MoS}_2$ cathode was alleviated and capacity was increased (Figure S7), resulting in a remarkable discharge capacity of 530 mAh g^{-1} in the 10th cycle.

To evaluate the rate capabilities, integrated cathode $0.85(0.8\text{Li}_2\text{S}-0.2\text{LiL})-0.15\text{MoS}_2$ was tested under different current densities of $25, 50, 100, 200 \text{ mA g}^{-1}$, shown in Figure 3b. The integrated $\text{Li}_2\text{S}-\text{LiL}-\text{MoS}_2$ cathode delivered discharge capacities of $530, 517, 473, 371 \text{ mAh g}^{-1}$, correspondingly with almost 100% of coulombic efficiency. The capacity retention was about 70% at 200 mA g^{-1} compared to the specific capacity at 25 mA g^{-1} . The long-term stability of $0.85(0.8\text{Li}_2\text{S}-0.2\text{LiL})-0.15\text{MoS}_2$ was also measured. As Figure S7 shows, there was no capacity decay after 500 cycles at 100 mA g^{-1} at 25°C , demonstrating superior long-term stability than reported sulfur-based cathodes that contain carbon and SE. The long-term stability of typical cathodes for all-solid-state Li-S batteries usually suffers from loss of contact between conductors and active materials due to volume change during the transformation between Li_2S and S_8 .^[16] Moreover, the conductive carbon causes degradation of SE in composite cathodes,^[17] which is evitable in our integrated $\text{Li}_2\text{S}-\text{LiL}-\text{MoS}_2$ cathode.

The $\text{Li}_2\text{S}-\text{LiL}-\text{MoS}_2$ cathode showed high capacity and low overpotential without solid electrolytes and carbon as additives into the composite, which is advantage for overall energy density.

Figure 3c shows, in the case of Li metal is anode, the comparison of power densities and energy densities based on the whole cathode of $0.85(0.8\text{Li}_2\text{S}-0.2\text{LiL})-0.15\text{MoS}_2$ with previous

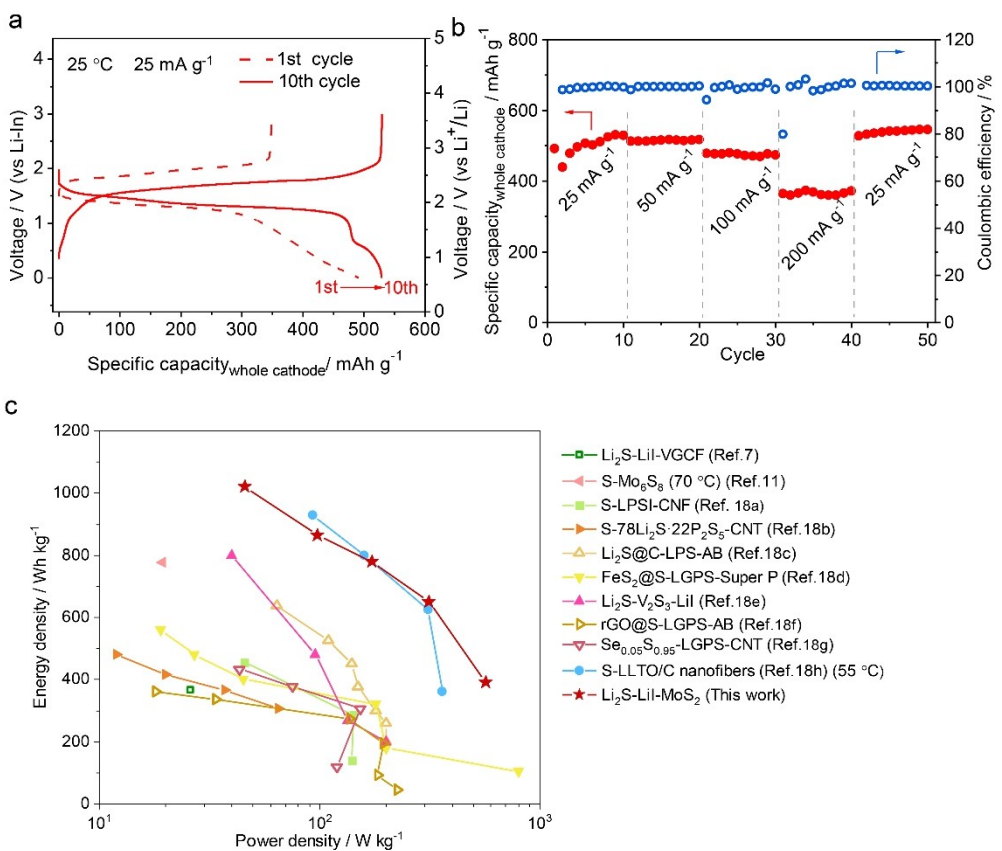


Figure 3. The electrochemical performance of 0.85(0.8Li₂S-0.2LiI)-0.15MoS₂. (a) The charge-discharge curves of 0.85(0.8Li₂S-0.2LiI)-0.15MoS₂ as cathode composite at 25 °C at the current density of 25 mA g⁻¹. (b) The rate performance and corresponding Coulombic efficiency. (c) Comparison of energy density and power density among different cathode composites for all-solid-state lithium-sulfur batteries and lithium metal as anode. The composite cathodes reported previously include Li₂S-Lil-vapor grown carbon fiber,^[7] S-Mo₆S₈,^[11] S-0.67Li₃PS₄,^[18a] 0.33LiI-carbon nano fiber,^[18b] S-78Li₂S·22P₂S₅-carbon nanotubes,^[18b] Li₂S@C-Li₂P₃S₁₁-acetylene black,^[18c] FeS₂@S-Li₁₀GeP₂S₁₂-Super P,^[18d] Li₂S-V₂S₃-Lil,^[18e] reduced graphene oxide@S-Li₁₀GeP₂S₁₂-acetylene black,^[18f] Se_{0.05}S_{0.95}-Li₁₀GeP₂S₁₂-carbon nanotubes,^[18g] and S-lithium lanthanum oxide/carbon nanofibers.^[18h]

cathode composites in ASSLSBs.^[7,11, 18] The integrated S-MoS₂-cathode reported previously shows relatively high energy density because of the absence of non-active conductors, under the condition of 70 °C and significantly low power density. Compared to these cathodes in ASSBs, 0.85(0.8Li₂S-0.2LiI)-0.15MoS₂ cathode in this work, shows a remarkably high energy density of 1020 Wh kg⁻¹ at 46 W kg⁻¹ under 25 °C, which delivers highest energy density among those of the cathodes for ASSLSBs with the same power density. Moreover, it shows 384 Wh kg⁻¹ with high power density of ~600 W kg⁻¹ at 25 °C, which is even better than the reported cathode based on sulfur with lithium lanthanum titanium oxide/carbon (LLTO/C) nanofibers at 55 °C. The superior energy density output under high power density of the Li₂S-Lil-MoS₂ cathode at room temperature demonstrates sufficient electron/ion supply in the all-solid-state composite electrode.

Understanding of the mechanism of the electrochemical reaction

As mentioned above, the 0.85(0.8Li₂S-0.2LiI)-0.15MoS₂ cathode after several cycles shows high energy density, compared to

previous cathode materials. To elucidate the charge compensation mechanism of the 0.85(0.8Li₂S-0.2LiI)-0.15MoS₂, Mo K-edge and S K-edge X-ray absorption spectroscopy (XAS) were conducted at different state of charge during 1st cycle and 5th cycle (Figure 4 and Figure S9). In Mo K-edge XAS of the 1st cycle, the absorption edge of the pristine sample slightly shifted to the lower energy compared to the starting material MoS₂ (2H-phase) (Figure S9b and S9c), which shows that the pristine sample was reduced lightly compared to the starting material MoS₂. This is probably due to the insertion of Li⁺ into MoS₂ and the formation of Li_xMoS₂ during ball milling process, which was proved by Raman and PDF analysis. The absorption edge shifted to the higher energy for charging to 100 mA h g⁻¹, and did not shift further with subsequent charge. This indicates that the Mo was oxidized due to the extraction of Li⁺ from Li_xMoS₂ until the charge of 100 mA h g⁻¹. After full discharge, the absorption edge shifted to the lower energy than that of the initial state, which shows a transition to a more reduced state. In the S K-edge XAS, the peak intensities at 2472.7 and 2475.4 eV attributed to Li₂S decreased, while the peak intensity at 2471.7 eV attributed to S₈ increased with charge process. This shows that a conversion reaction from Li₂S to S₈ occurred during charge process.^[19] After full discharge, the peak intensity

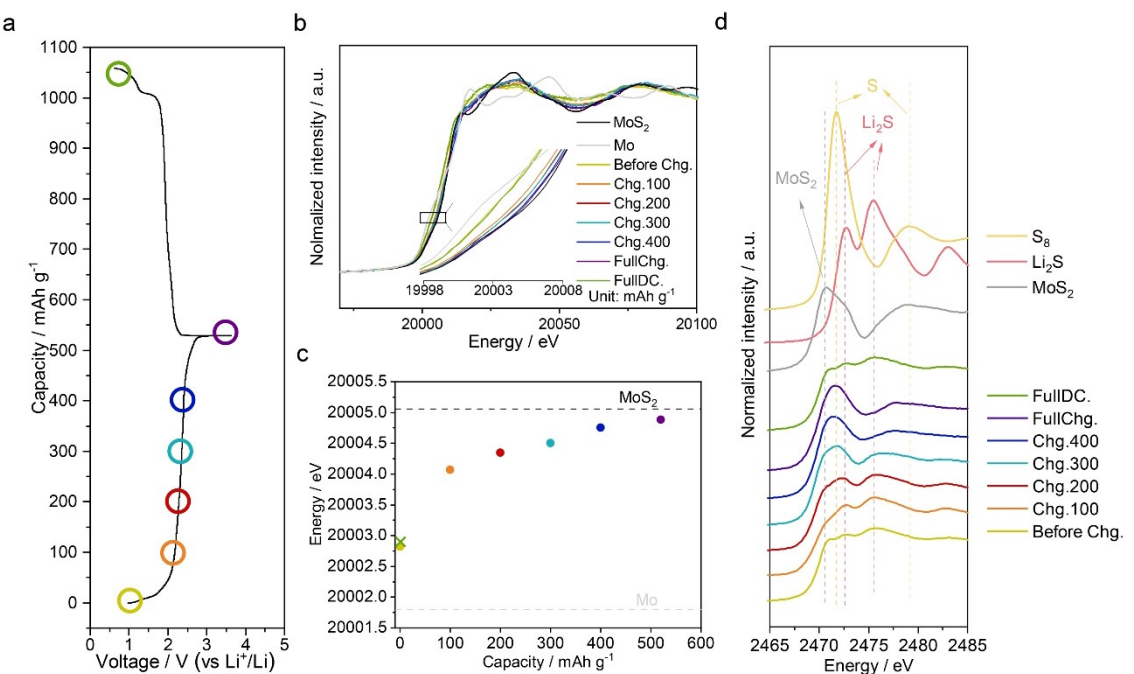


Figure 4. Mechanism of electrochemical reaction of 0.85(0.8Li₂S-0.2LiI)-0.15MoS₂ cathode during the fifth cycle. (a) The 5th charge-discharge curves of 0.85(0.8Li₂S-0.2LiI)-0.15MoS₂ cathode. (b) Mo K-edge XANES of 0.85(0.8Li₂S-0.2LiI)-0.15MoS₂ cathode at different state of charge. (c) Enlarged part of Figure 4b about absorption energies for Li₂S-LiI-MoS₂ cathode, which delivers different capacities. Circle marks correspond to before charge and charge state, and the cross mark corresponds to the difference between fifth charge capacity and discharge capacity. (d) S K-edge XANES of 0.85(0.8Li₂S-0.2LiI)-0.15MoS₂ cathode at different state of charge.

at 2470.6 eV attributed to MoS₂ decreased and the peak intensities at 2472.7 and 2475.4 eV attributed to Li₂S increased. Compared to the initial state, the large reduction of Mo and the significant change in the electronic structure of S attributed to MoS₂ after discharge indicate insertion of Li⁺ into the 1T-Li_xMoS₂ in the 0.85(0.8Li₂S-0.2LiI)-0.15MoS₂. This reaction results in the higher initial discharge capacity than the charge capacity.

In Mo K-edge XAS of the 5th cycle (Figure 4b and c), the absorption edge of the sample before charge substantially shifted to the higher energy for charging to 100 mAh g⁻¹, and gradually shifted further for subsequent charging. This indicates that the Mo largely contributed to the charge compensation with the charge of 100 mAh g⁻¹ and the contribution became relatively small after the charge state of 100 mAh g⁻¹. As for the full discharge, the absorption edge returned to the same energy as the pristine sample, which shows the Mo redox occurred reversibly. In the S K-edge XAS of the 5th cycle (Figure 4d), one peak attributed to MoS₂ was observed at 2470.6 eV, and two peaks attributed to Li₂S were observed at 2472.7 and 2475.4 eV in the sample before charging. The intensity of peak at 2470.6 eV decreased for charging to 100 mAh g⁻¹, which may be caused by largely oxidation of Mo (Figure 4b and c). During the subsequent charge process, the peak intensities at 2472.7 and 2475.4 eV attributed to Li₂S decreased while the peak intensity at 2471.7 eV attributed to S₈ increased. This shows a conversion reaction from Li₂S to S₈ during charging. After discharge, the XANES shape was similar to that of the pristine sample, which shows the S redox occurred reversibly. The capacity contribution of 1T-MoS₂ is calculated by combining the

theoretical capacity of MoS₂ and assuming the real reacted electron number of MoS₂ based on Mo K-edge XANES. The theoretical capacity of MoS₂ with a 4-electron transfer reaction is 670 mAh g⁻¹, based on the reaction MoS₂+4Li⁺+4e⁻→Mo+Li₂S. Considering the MoS₂ content in 85(80Li₂S-20LiI)-15MoS₂, the capacity contribution of 1T-MoS₂ is no more than 206 mAh g⁻¹. The actual reacted electron can be inferred by assuming a linear relationship between the oxidation number of Mo and the energy of Mo K-edge XANES. As Figure S10 shows, about 2.4 electrons participate in the reaction, corresponding to the capacity of 125 mAh g⁻¹, which is also in good agreement with the capacity related to the second voltage plateau starting at about 1.1 V vs. Li⁺/Li in the discharge curve (Figure 4a). Both Mo K-edge and S K-edge XAS spectra prove the reversible cationic redox of Mo and anionic redox of S, which leads to the high energy density and reversibility of the 0.85(0.8Li₂S-0.2LiI)-0.15MoS₂ cathode.

Understanding of the power density

The 0.85(0.8Li₂S-0.2LiI)-0.15MoS₂ cathode shows high power density as well as high energy density, compared to previous cathode materials. To clarify the reason for the high power density, apparent ionic conductivity, crystal structure and morphology of the 0.85(0.8Li₂S-0.2LiI)-0.15MoS₂ during charge/discharge processes were examined. The apparent ionic conductivity of the 0.85[(1-x)Li₂S-xLiI]-0.15MoS₂ ($x=0.05, 0.10, 0.15, 0.20, 0.25$) cathodes was measured using a potential step

method combined with the Cottrell and Nernst–Einstein equations (Figure 5a and S11). The apparent ionic conductivity increased with the LiI content until $x=0.20$, and the value at $x=20$ ($0.85(0.8\text{Li}_2\text{S}-0.2\text{LiI})-0.15\text{MoS}_2$) was $6.6 \times 10^{-5} \text{ S cm}^{-1}$. This result shows that the $0.85(0.8\text{Li}_2\text{S}-0.2\text{LiI})-0.15\text{MoS}_2$ cathode has relatively high ionic conductivity even after first charge process, which leads to the high power density of the cathode. Structural change for $0.85(0.8\text{Li}_2\text{S}-0.2\text{LiI})-0.15\text{MoS}_2$ upon the first cycle was examined by synchrotron XRD (Figure 5b). Before charging, all Bragg peaks were assigned to Li_2S (space group: $Fm\bar{3}m$) and In (space group: $I4/mmm$), which was impurity from the anode in the XRD sample preparation procedure. During charging, the intensity of the peaks attributed to the Li_2S structure decreased while new peaks attributed to LiI (space group: $Fm\bar{3}m$) appeared with stronger intensity as the charging proceeded. In the subsequent discharge, the intensity of the peaks attributed to the Li_2S structure increased while the LiI peaks remained with decreased intensity. These results show LiI phase formed from the Li_2S -LiI solid solution in the $0.85(0.8\text{Li}_2\text{S}-0.2\text{LiI})-0.15\text{MoS}_2$ during the first charge and could keep in the cathode after first cycle. In addition, the peaks of LiI remain visible after the second and fifth cycles, indicating the good stability of LiI phase in $0.85(0.8\text{Li}_2\text{S}-0.2\text{LiI})-0.15\text{MoS}_2$ cathode after the second and fifth cycle (shown in Figure S12).

The formed LiI phase and its morphology were further confirmed by Computed Tomography (CT) (Figure 5c–f). These CT images approximately represent the density distribution of the object. Before charging, as all elements were uniformly

distributed in the $0.85(0.8\text{Li}_2\text{S}-0.2\text{LiI})-0.15\text{MoS}_2$ (Figure S13), no contrast was observed in the CT image except in the void areas (Figure 5c), which were regions of low density (blank). During charge process, region with high density (blue color) appeared and increased uniformly with charging. In the subsequent discharge, the region with high density remained although the region was decreased. Considering the XRD results (Figure 5b), the region with high density is attributed to the formation of LiI from Li_2S -LiI solid solution.

It has been reported that the formed LiI domain can work as an ionic conduction path in other LiI doped cathodes to suppress decreasing the ionic conductivity of cathodes during charging.^[20] Meanwhile, as for the aspect of electronic conductivity, the $0.85(0.8\text{Li}_2\text{S}-0.2\text{LiI})-0.15\text{MoS}_2$ cathode possesses good electronic transportability at pristine state, which is due to the good electronic conductivity of 1T- MoS_2 ($10-100 \text{ S cm}^{-1}$).^[21] It is reported that the high electronic conductivity is because the electronic states of 1T- MoS_2 around Fermi level are composed of partially filled Mo 4d and S 3p states, which is based on the results of the density of states (DOS).^[22] Moreover, with the different electric charge of Mo in 1T MoS_2 , the shape of DOS patterns remains nearly unchanged,^[23] which indicates the lithiated $\text{Li}_{x}\text{MoS}_2$ could keep electronic conductivities as high as 1T- MoS_2 during charge and discharge. Resulting from high electronic and ionic conductivities at pristine state, stably high electronic conductivity of $\text{Li}_{x}\text{MoS}_2$ and the high apparent ionic conductivity originated from the formed LiI domain during charging, the integrated $0.85(0.8\text{Li}_2\text{S}-0.2\text{LiI})-0.15\text{MoS}_2$ cathode

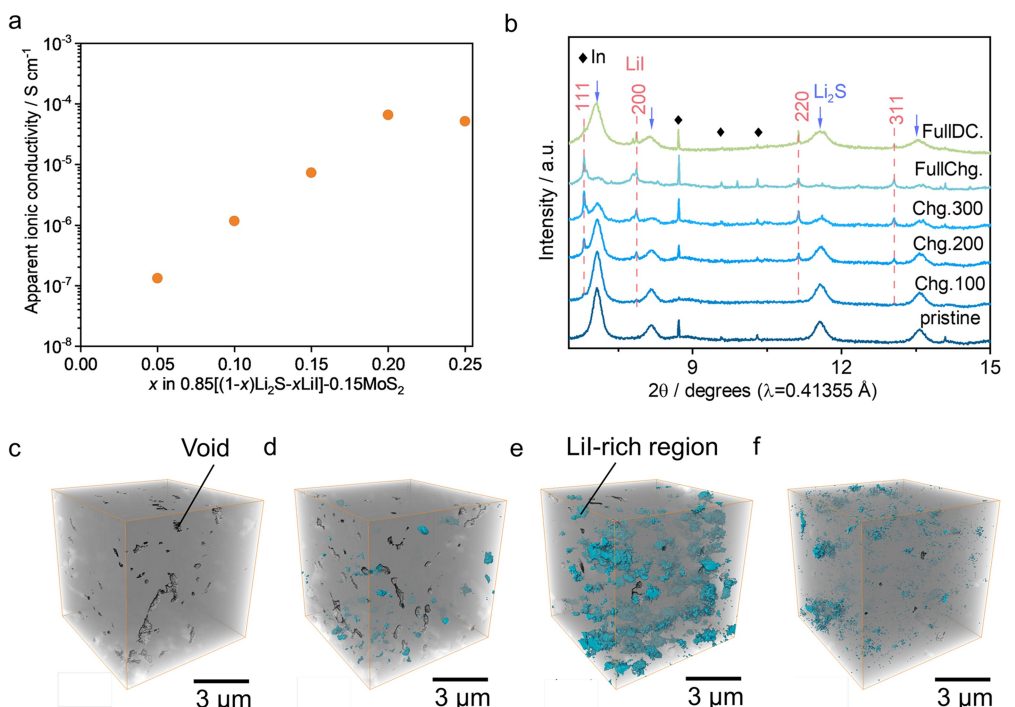


Figure 5. The function of LiI in Li_2S -LiI- MoS_2 . (a) The apparent ionic conductivities at full charge state of $0.85[(1-x)\text{Li}_2\text{S}-x\text{LiI}]-0.15\text{MoS}_2$ at 25°C . (b) Synchrotron XRD patterns of $0.85(0.8\text{Li}_2\text{S}-0.2\text{LiI})-0.15\text{MoS}_2$ at pristine state, charge state with cut-off capacity of 100, 200 and 300 mAh g^{-1} , full-charge state and full-discharge state at the 1st cycle. The pink dash lines point to the position of LiI. The peaks of Indium are marked as diamonds. The blue arrows correspond to Li_2S -type phase. Computed Tomography (CT) of $0.85(0.8\text{Li}_2\text{S}-0.2\text{LiI})-0.15\text{MoS}_2$ cathode at (c) pristine (d) cut-off at 175 mAh g^{-1} (equal to half of first full charge capacity) (e) full-charge (f) full-discharge state. Blank parts and blue regions indicated correspond to the voids and LiI-rich domains in $0.85(0.8\text{Li}_2\text{S}-0.2\text{LiI})-0.15\text{MoS}_2$ cathode, respectively.

realize remarkable energy density and high power density without carbon and SE in the cathode composite.

Conclusions

In summary, we have successfully synthesized $\text{Li}_2\text{S}-\text{Lil}-\text{MoS}_2$ integrated cathode with high electronic and ionic conductivities over $10^{-4} \text{ S cm}^{-1}$ by one-step ball-milling method. Without any carbon and solid electrolytes additives in cathode composite, the optimized $\text{Li}_2\text{S}-\text{Lil}-\text{MoS}_2$ integrated cathode ($0.85(0.8\text{Li}_2\text{S}-0.2\text{Lil})-0.15\text{MoS}_2$) delivers the highest energy density of 1020 Wh kg^{-1} at the cathode level and superior power density to other cathodes for ASSLSB. The utilization of the reversible cationic redox of Mo and anionic redox of S in the $0.85(0.8\text{Li}_2\text{S}-0.2\text{Lil})-0.15\text{MoS}_2$ cathode leads to the high energy density. The high electronic and ionic conductivities at pristine state and the formed Lil domain during charging lead to the high power density. The design strategy used in the $\text{Li}_2\text{S}-\text{Lil}-\text{MoS}_2$ is useful to realize ASSBs with high energy and power densities.

Experimental Section

Material synthesis

The $(1-x)\text{Li}_2\text{S}-x\text{Lil}$ ($x = 0.05, 0.1, 0.15, 0.2, 0.25$) and $(1-y)(0.8\text{Li}_2\text{S}-0.2\text{Lil})-y\text{MoS}_2$ ($x=0, 0.05, 0.1, 0.15, 0.2$) samples in this study were prepared using ball milling. Stoichiometric amounts of Li_2S (99% purity, Mitsuwa), MoS_2 (99% purity, Kojundo), and Lil (99% purity, Aldrich) were hand-mixed in a mortar for 0.5 h, followed by mechanical mixing with ZrO_2 balls at 530 rpm for 80 h. The Li_3PS_4 glass powder used to fabricate the SE was prepared via ball milling using a previously reported procedure, as follows.^[24] Li_2S (99% purity, Aldrich) and P_2S_5 (99% purity, Aldrich) powders with a 3:1 molar ratio were mechanically mixed using ZrO_2 balls at 600 rpm for 16 h. All experiments were performed in a dry Ar-filled glovebox.

Material characterization

The synchrotron X-ray diffraction (XRD) profiles of the as-prepared The $(1-x)\text{Li}_2\text{S}-x\text{Lil}$ ($x=0.05, 0.1, 0.15, 0.2, 0.25$) and $(1-y)(0.8\text{Li}_2\text{S}-0.2\text{Lil})-y\text{MoS}_2$ ($x=0, 0.05, 0.1, 0.15, 0.2$) cathode materials and Pair Distribution Function (PDF) were obtained at the BL02B2 beamline of SPring-8, Japan. Rietveld structure refinements using GSAS program and PDF analysis using PDF gui were carried out.^[25]

Raman measurements in the $100-500 \text{ cm}^{-1}$ range were performed using a DXR3 Smart Raman spectrometer (Thermo Fisher Scientific) with a 532 nm diode-pumped solid-state laser at room temperature. The scanning electron microscopy (SEM) images and energy dispersive X-ray spectroscopy (EDX) profiles of the as-prepared $0.85(0.8\text{Li}_2\text{S}-0.2\text{Lil})-0.15\text{MoS}_2$ were recorded using Hitachi's SU-8200 series cold field emission scanning electron microscopy device.

The X-ray absorption spectroscopy (XAS) of Mo K -edge for the cathode materials were recorded at BL14B2 beamline of the SPring-8, Japan. The S K -edge and Mo L -edge of the cathode materials were recorded at the BL6N1 beamline of the Aichi Synchrotron Radiation Center, Japan. X-ray CT analysis of the cathode materials was performed using a phase-contrast method at the BL20XU beamline of the SPring-8, Japan.^[26] The voxel size of the reconstructed images was 62.4 nm. XAS and CT analyses were

performed after the cells were disassembled in a dry Ar-filled glovebox following galvanostatic measurements without exposing the cathode materials to air.

Electrochemical measurements

The electrochemical performance of the $0.85[(1-x)\text{Li}_2\text{S}-x\text{Lil}]-0.15\text{MoS}_2$ and $(1-y)(0.8\text{Li}_2\text{S}-0.2\text{Lil})-y\text{MoS}_2$ cathode materials was analyzed using a two-electrode cell. The $(1-x)(0.8\text{Li}_2\text{S}-0.2\text{Lil})-x\text{MoS}_2$ and $0.85[(1-y)\text{Li}_2\text{S}-y\text{Lil}]-0.15\text{MoS}_2$ composites were used as cathode materials without adding conductive materials and SE to them, and the prepared Li_3PS_4 was used as the solid-state electrolyte (SE) of the cell. The $0.85[(1-x)\text{Li}_2\text{S}-x\text{Lil}]-0.15\text{MoS}_2$ and $(1-y)(0.8\text{Li}_2\text{S}-0.2\text{Lil})-y\text{MoS}_2$ cathode materials with 4 mg mass loading (corresponding to $\sim 30 \mu\text{m}$ of thickness) and the SE layer with 80 mg were placed in a polycarbonate tube with a diameter of 10 mm and were pressed together under a pressure of 360 MPa. A Li–In alloy layer was placed on the SE layer at the opposite side to the cathode layer and served as the anode.^[27] Two stainless-steel rods, which were added to the cathode and anode sides by applying a pressure of 120 MPa, were used as current collectors. Cell assembly was performed in a dry Ar-filled glovebox. Electrochemical tests were performed at a current density of 25 mA g^{-1} with discharge and charge cutoff voltages of 0 (0.62 V vs. Li^+/Li) and 3.0 V (3.62 V),^[28] respectively, at 25°C .

To measure the electronic and ionic conductivities of the $0.85[(1-x)\text{Li}_2\text{S}-x\text{Lil}]-0.15\text{MoS}_2$ and $(1-y)(0.8\text{Li}_2\text{S}-0.2\text{Lil})-y\text{MoS}_2$ composites, direct current (DC) polarization and alternating current (AC) impedance were measured, respectively. The cathode materials were pressed into pellets under a pressure of 360 MPa and set between two stainless-steel current collectors. The applied voltage for DC polarization using HZ-7000 (Hokuto Denko) is 1 V and maintained 0.5 h to obtain the stable current. During the test, the mold was under 120 MPa pressure for the good contact between the pellet sample and current collectors. The electronic conductivity is calculated following $\sigma = \frac{L}{RS} = \frac{I}{SV}$, where R is the resistance of $\text{Li}_2\text{S}-\text{Lil}-\text{MoS}_2$, which can be calculated by corresponding current and applied voltage, I is the stable current, L is the thickness of $\text{Li}_2\text{S}-\text{Lil}-\text{MoS}_2$ pellet, V is the applied voltage and S is the cross-sectional area of the pellet. As for the measurement of ionic conductivities, $\text{Li}_2\text{S}-\text{Lil}-\text{MoS}_2$ was first pressed into a pellet in a mold, the same as the electronic conductivity measurement procedure. Then Li_3PS_4 , a common solid-state electrolyte with good ionic conductivity ($10^{-4} \text{ S cm}^{-1}$) and negligible electronic conductivity ($10^{-8} \text{ S cm}^{-1}$),^[29] was used as the electron blocking layer on both sides of $\text{Li}_2\text{S}-\text{Lil}-\text{MoS}_2$ pellet. The total impedance of $\text{Li}_3\text{PS}_4|\text{Li}_2\text{S}-\text{Lil}-\text{MoS}_2|\text{Li}_3\text{PS}_4$ was measured by Modulab XM ECS using alternating current (AC) impedance technique. The AC amplitude was 10 mV, and the applied frequency ranged between 1 MHz and 0.1 Hz. By subtracting the impedance of Li_3PS_4 from the total impedance, the impedance of $\text{Li}_2\text{S}-\text{Lil}-\text{MoS}_2$ can be obtained and used to calculate the corresponding ionic conductivity.

To measure the lithium ion diffusion coefficient of the $0.85[(1-x)\text{Li}_2\text{S}-x\text{Lil}]-0.15\text{MoS}_2$ and $(1-y)(0.8\text{Li}_2\text{S}-0.2\text{Lil})-y\text{MoS}_2$ cathode materials, we used a potential step method. A constant potential of 3.0 V was applied to the cells, and the time dependence of the current was monitored using the Modulab XM ECS (Solartron Analytical). The apparent diffusion coefficients of the composite cathode materials were calculated using the Cottrell equation:

$$i = \frac{nFAD^{1/2}C}{\sqrt{\pi t}},$$

where i is the current, n is the number of electrons, F is the Faraday constant, A is the geometric area, D is the diffusion coefficient, C is the lithium ion concentration, and t is the time. The apparent ionic conductivity of the cathode composites during the potential step was estimated using the Nernst – Einstein equation:

$$\sigma = \frac{CZ^2F^2D}{RT},$$

where σ is the ionic conductivity, Z is the charge valence, R is the gas constant, and T is the absolute temperature.

Acknowledgements

This research was supported by JST, ALCA-SPRING Project (Grant Number: JPMJAL1301). Synchrotron radiation experiments were performed at beam line BL02B2, BL14B2 and BL20XU at SPring-8 with the approval of the JASRI (Proposal numbers 2020A0664, 2022A1781 and 2022A1033) and BL6N1 at Aichi SR (Proposal numbers 202206124). Acknowledgements are also issued to China Scholarship Council (No. 202208050074) and Kyoto University for their financial support to W. Pan.

Conflict of Interests

The authors declare no conflict of interest.

Data Availability Statement

The data that support the findings of this study are available from the corresponding author upon reasonable request.

Keywords: all-solid-state lithium-sulfur batteries • ionic-electronic conductive cathodes • synchrotron X-ray analyses

- [1] a) Y. Huang, L. Lin, C. Zhang, L. Liu, Y. Li, Z. Qiao, J. Lin, Q. Wei, L. Wang, Q. Xie, *Adv. Sci.* **2022**, *9*, 2106004; b) J. Jiang, Q. Fan, S. Chou, Z. Guo, K. Konstantinov, H. Liu, J. Wang, *Small* **2021**, *17*, 1903934.
- [2] a) X. Yang, J. Luo, X. Sun, *Chem. Soc. Rev.* **2020**, *49*, 2140; b) L.-P. Hou, X.-Q. Zhang, B.-Q. Li, Q. Zhang, *Mater. Today* **2021**, *45*, 62; c) B. Liu, J.-G. Zhang, W. Xu, *Joule* **2018**, *2*, 833.
- [3] a) H. Lee, P. Oh, J. Kim, H. Cha, S. Chae, S. Lee, J. Cho, *Adv. Mater.* **2019**, *31*, 1900376; b) Y.-X. Song, Y. Shi, J. Wan, S.-Y. Lang, X.-C. Hu, H.-J. Yan, B. Liu, Y.-G. Guo, R. Wen, L.-J. Wan, *Energy Environ. Sci.* **2019**, *12*, 2496.
- [4] B. Ding, J. Wang, Z. Fan, S. Chen, Q. Lin, X. Lu, H. Dou, A. K. Nanjundan, G. Yushin, X. Zhang, *Mater. Today* **2020**, *40*, 114.
- [5] a) H. Nagata, Y. Chikusa, *J. Power Sources* **2014**, *264*, 206; b) K. Suzuki, D. Kato, K. Hara, T.-a. Yano, M. Hirayama, M. Hara, R. Kanno, *Electrochim. Acta* **2017**, *258*, 110.
- [6] F. Wu, J. T. Lee, N. Nitta, H. Kim, O. Borodin, G. Yushin, *Adv. Mater.* **2015**, *27*, 101.
- [7] T. Hakari, A. Hayashi, M. Tatsumisago, *Adv. Sustainable Syst.* **2017**, *1*, 1700017.
- [8] a) H. Wan, B. Zhang, S. Liu, J. Zhang, X. Yao, C. Wang, *Nano Lett.* **2021**, *21*, 8488; b) R. Xu, J. Yue, S. Liu, J. Tu, F. Han, P. Liu, C. Wang, *ACS Energy Lett.* **2019**, *4*, 1073.
- [9] a) X. Liu, J. Q. Huang, Q. Zhang, L. Mai, *Adv. Mater.* **2017**, *29*, 1601759; b) W. Xue, Z. Shi, L. Suo, C. Wang, Z. Wang, H. Wang, K. P. So, A. Maurano, D. Yu, Y. Chen, *Nat. Energy* **2019**, *4*, 374; c) K. Liang, K. Marcus, S. Zhang, L. Zhou, Y. Li, S. T. De Oliveira, N. Orlovskaya, Y. H. Sohn, Y. Yang, *Adv. Energy Mater.* **2017**, *7*, 1701309; d) Q. Luo, R. Tian, A. Wu, X. Dong, X. Jin, S. Zhou, H. Huang, *Mater. Today Energy* **2020**, *17*, 100439; e) H. Xu, A. Manthiram, *Nano Energy* **2017**, *33*, 124.
- [10] a) U. Ulissi, S. Ito, S. M. Hosseini, A. Varzi, Y. Aihara, S. Passerini, *Adv. Energy Mater.* **2018**, *8*, 1801462; b) S. Xu, C. Y. Kwok, L. Zhou, Z. Zhang, I. Kochetkov, L. F. Nazar, *Adv. Funct. Mater.* **2021**, *31*, 2004239.
- [11] M. Li, T. Liu, Z. Shi, W. Xue, Y. s. Hu, H. Li, X. Huang, J. Li, L. Suo, L. Chen, *Adv. Mater.* **2021**, *33*, 2008723.
- [12] a) T. Wang, J. Zhu, Z. Wei, H. Yang, Z. Ma, R. Ma, J. Zhou, Y. Yang, L. Peng, H. Fei, *Nano Lett.* **2019**, *19*, 4384; b) Y. Lu, X. Huang, Z. Song, K. Rui, Q. Wang, S. Gu, J. Yang, T. Xiu, M. E. Badding, Z. Wen, *Energy Storage Mater.* **2018**, *15*, 282.
- [13] a) Y. Jiao, A. M. Hafez, D. Cao, A. Mukhopadhyay, Y. Ma, H. Zhu, *Small* **2018**, *14*, e1800640; b) X. Geng, W. Sun, W. Wu, B. Chen, A. Al-Hilo, M. Benamarra, H. Zhu, F. Watanabe, J. Cui, T. P. Chen, *Nat. Commun.* **2016**, *7*, 10672; c) E. Er, H.-L. Hou, A. Criado, J. Langer, M. Möller, N. Erk, L. M. Liz-Marzán, M. Prato, *Chem. Mater.* **2019**, *31*, 5725.
- [14] Z. Lei, J. Zhan, L. Tang, Y. Zhang, Y. Wang, *Adv. Energy Mater.* **2018**, *8*, 1703482.
- [15] J. Bai, B. Zhao, J. Zhou, J. Si, Z. Fang, K. Li, H. Ma, J. Dai, X. Zhu, Y. Sun, *Small* **2019**, *15*, 1805420.
- [16] S. Ohno, R. Koerver, G. Dewald, C. Rosenbach, P. Titscher, D. Steckermeier, A. Kwade, J. r. Janek, W. G. Zeier, *Chem. Mater.* **2019**, *31*, 2930.
- [17] S. Ohno, C. Rosenbach, G. F. Dewald, J. Janek, W. G. Zeier, *Adv. Funct. Mater.* **2021**, *31*, 2010620.
- [18] a) N. H. H. Phuc, M. Takaki, H. Muto, M. Reiko, H. Kazuhiro, A. Matsuda, *ACS Appl. Energ. Mater.* **2020**, *3*, 1569; b) Y. Zhang, T. Liu, Q. Zhang, X. Zhang, S. Wang, X. Wang, L. Li, L.-Z. Fan, C.-W. Nan, Y. Shen, *J. Mater. Chem. A* **2018**, *6*, 23345; c) H. Yan, H. Wang, D. Wang, X. Li, Z. Gong, Y. Yang, *Nano Lett.* **2019**, *19*, 3280; d) J. P. Mwizerwa, Q. Zhang, F. Han, H. Wan, L. Cai, C. Wang, X. Yao, *ACS Appl. Mater. Interfaces* **2020**, *12*, 18519; e) T. Shigedomi, Y. Fujita, T. Kishi, K. Motohashi, H. Tsukasaki, H. Nakajima, S. Mori, M. Tatsumisago, A. Sakuda, A. Hayashi, *Chem. Mater.* **2022**, *34*, 9745; f) X. Yao, N. Huang, F. Han, Q. Zhang, H. Wan, J. P. Mwizerwa, C. Wang, X. Xu, *Adv. Energy Mater.* **2017**, *7*, 1602923; g) Y. Zhang, Y. Sun, L. Peng, J. Yang, H. Jia, Z. Zhang, B. Shan, J. Xie, *Energy Storage Mater.* **2019**, *21*, 287; h) L. Wang, X. Yin, B. Li, G. W. Zheng, *Nano Lett.* **2022**, *22*, 433.
- [19] a) L. Zhang, D. Sun, J. Feng, E. J. Cairns, J. Guo, *Nano Lett.* **2017**, *17*, 5084; b) S. F. Ng, M. Y. L. Lau, W. J. Ong, *Adv. Mater.* **2021**, *33*, 2008654.
- [20] a) T. Shigedomi, Y. Fujita, T. Kishi, K. Motohashi, H. Tsukasaki, H. Nakajima, S. Mori, M. Tatsumisago, A. Sakuda, A. Hayashi, *Chem. Mater.* **2022**, *34*, 9745; b) K. Yamamoto, Y. Xiao, T. Watanabe, A. Sakuda, M. Takahashi, W. Pan, K. Nakanishi, T. Matsunaga, M. Uesugi, A. Takeuchi, K. Uesugi, A. Hayashi, M. Tatsumisago, Y. Uchimoto, *J. Phys. Chem. C* **2023**, *127*, 14656.
- [21] M. Acerce, D. Voiry, M. Chhowalla, *Nat. Nanotechnol.* **2015**, *10*, 313.
- [22] Q. Tang, D.-e. Jiang, *Chem. Mater.* **2015**, *27*, 3743.
- [23] Q. Huang, J. Shen, Y. Lu, R. Ye, S. Gong, *J. Phys. Chem. C* **2023**, *127*, 17406.
- [24] K. Yamamoto, S. Yang, M. Takahashi, K. Ohara, T. Uchiyama, T. Watanabe, A. Sakuda, A. Hayashi, M. Tatsumisago, H. Muto, *ACS Appl. Energ. Mater.* **2021**, *4*, 2275.
- [25] a) B. H. Toby, *J. Appl. Crystallogr.* **2001**, *34*, 210; b) C. Farrow, P. Juhas, J. Liu, D. Bryndin, E. Božin, J. Bloch, T. Proffen, S. Billinge, *J. Phys. Condens. Matter* **2007**, *19*, 335219.
- [26] A. Takeuchi, K. Uesugi, M. Uesugi, H. Toda, K. Hirayama, K. Shimizu, K. Matsuo, T. Nakamura, *Rev. Sci. Instrum.* **2021**, *92*, 023701.
- [27] a) M. Nagao, A. Hayashi, M. Tatsumisago, *Electrochim. Acta* **2011**, *56*, 6055; b) A. Santhosh, L. Medenbach, J. R. Buchheim, P. Adelhelm, *Batteries & Supercaps* **2019**, *2*, 524.
- [28] K. Takada, N. Aotani, K. Iwamoto, S. Kondo, *Solid State Ionics* **1996**, *86*, 877.
- [29] Ö. U. Kudu, T. Famprakis, S. Cretu, B. Porcheron, E. Salager, A. Demortiere, M. Courty, V. Viallet, T. L. Mercier, B. Fleutot, M.-D. Braida, C. Masquelier, *Energy Storage Mater.* **2022**, *44*, 168.

Manuscript received: October 18, 2023

Revised manuscript received: October 26, 2023

Accepted manuscript online: October 27, 2023

Version of record online: November 20, 2023